ACS OMEGA

http://pubs.acs.org/journal/acsodf

Article

Laser-Induced Carbon Electrodes in a Three-Dimensionally Printed Flow Reactor for Detecting Lead Ions

Baojun Ding,‡ Qiunan Zhang,‡ Cheng Yang,‡ Wenbo Yang, Junbo Liu, Chong Li, and Shengyang Tao*

Cite This: *ACS Omega* 2021, 6, 12470−12479

Read Online

ACCESS | Metrics & More | Article Recommendations

ABSTRACT: Nowadays, heavy metal pollution has attracted wide attention. Many electrochemical methods have been developed to detect heavy metal ions. The electrode surface usually needs to be modified, and the process is complicated. Herein, we demonstrate the fabrication of electrodes by direct laser sintering on commercial polymer films. The prepared porous carbon electrodes can be used directly without any modification. The electrodes were fixed in a 3D-printed flow reactor, which led to very little analyte required during the detection process. The velocities of the analyte under stirring and flowing conditions were simulated numerically. The results prove that flow detection is more conducive to improving detection sensitivity. The limit of detection is about 0.0330 mg/L for Pb^{2+}. Moreover, the electrode has been proved to have good repeatability and stability.

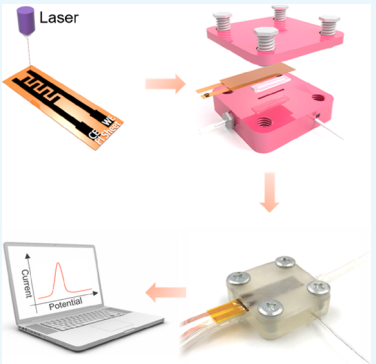

1. INTRODUCTION

With the rapid development of economy and technology, the pollution of heavy metals such as lead ions has caused widespread concern.[1] Pb^{2+} is a kind of toxic heavy metal ion that is harmful to human health and can damage the nervous and digestive systems. Lead poisoning can cause intellectual and developmental problems.[2,3] For human health, the detection and analysis of heavy metal ions are critical. At present, the detection methods of lead ions mainly include absorption photometry, atomic absorption spectroscopy, atomic fluorescence spectrometry, inductively coupled plasma atomic emission spectrometry, X-ray fluorescence spectrometry, and mass spectrometry.[4−7] Although these methods are very sensitive, they have some disadvantages, such as expensive equipment, complex preprocessing, long-time consumption, and poor real-time detection.

Compared with other detection methods, electrochemical detection has the advantages of fast analysis speed, high sensitivity, simple operation, low detection cost, and no requirement of expensive large-scale instruments. It is widely used in the detection of heavy metal ions.[8−11] The most commonly used electrochemical detection technique is voltammetry, including cyclic voltammetry (CV), linear scanning voltammetry (LSV), anode stripping voltammetry (ASV), square wave voltammetry (SWV), and differential pulse voltammetry (DPV).[12−14] In ion trace analysis, the most common detection method is stripping voltammetry, which combines the constant potential analysis with the voltammetric analysis.[15] The analysis method has two steps. The first step is to make the analyte perform constant potential electrolysis in the stirred state, which will make the analyte be reduced and deposited on the cathode. This process is called the enrichment process. The second step is to apply a reverse scanning voltage to the electrode after a period of quiescence so that the analyte deposited on the cathode is oxidized and redissolved in the solution. This process is called the stripping process.[16,17] Compared with the direct voltammetric analysis of the original solution, the biggest advantage of this method is that the analyte can be pre-enriched on the electrode, so the dissolution current is not affected by the charging current and the impurity residual current.

Metal oxides, expensive metals, and carbon are often used as electrodes for detecting heavy metal ions.[18,19] But metal oxide has low conductivity. Noble metals are scarce, and their high price limits their widespread use. However, as one of the most common elements in nature, carbon has good biocompatibility and is a kind of a low-consumption material,[20,21] so it is often used to make electrodes. Traditional carbon materials are activated carbon, graphite, carbon nanotubes, and graphene. To improve material performance, researchers have introduced the concept of porosity into the construction of carbon materials. Porous carbon has many advantages, such as a large

Received: December 25, 2020
Accepted: April 28, 2021
Published: May 4, 2021

https://doi.org/10.1021/acsomega.0c06274
ACS Omega 2021, 6, 12470−12479

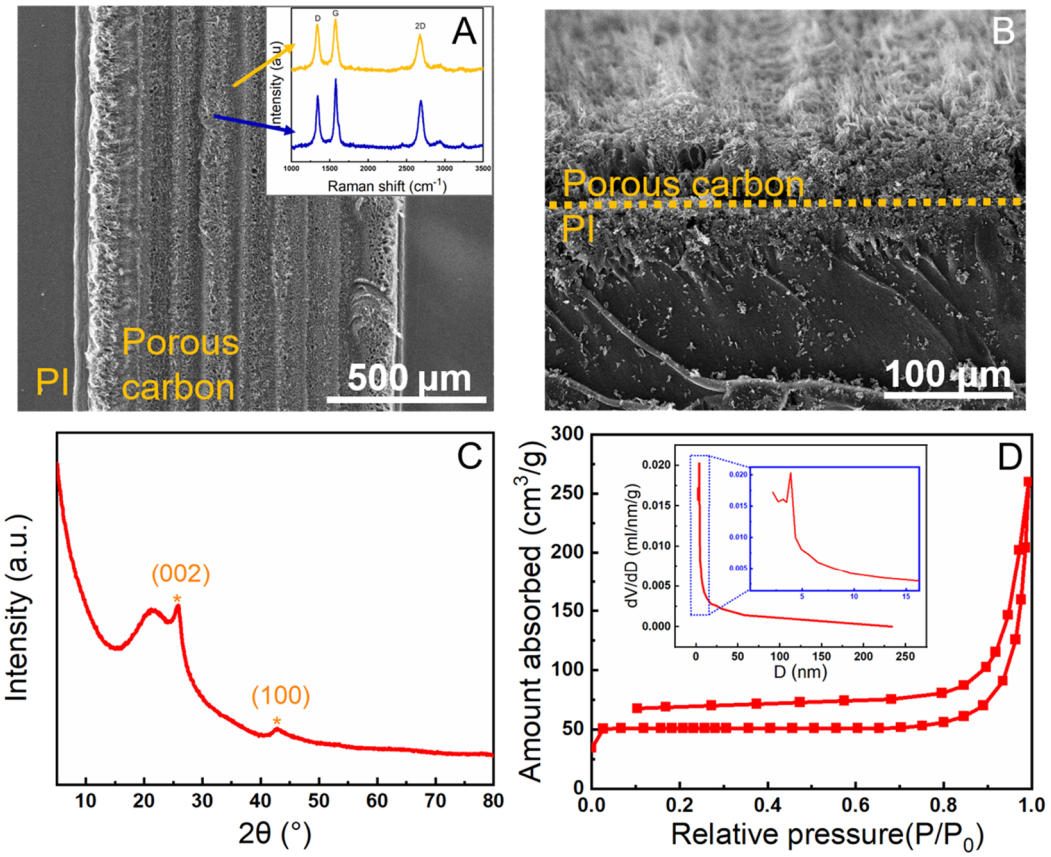

Figure 1. Characterization of LIPC. (A) SEM image of LIPC. The scale bar is 500 μm. The inset is the Raman spectra of carbon on the region of the laser scratch track and between the two tracks. (B) Cross-sectional SEM image of LIPC on the PI film. The scale bar is 100 μm. (C) XRD of powdered LIPC scraped from the PI film. (D) N_2 adsorption−desorption isotherm of powdered LIPC scraped from the PI film. The inset is the PSD of the sample calculated from the desorption isotherm.

specific surface area, good conductivity, and many active sites. It is a very suitable electrode material.[22]

Herein, porous carbon electrodes were prepared by CO_2 infrared laser sintering on commercial polymer films. The process is simple to operate and is a new manufacturing technology, which significantly improves production efficiency and reduces costs. Tour *et al.* used this technique to make polymer-written electronic and energy storage devices.[23] The application of this technology in microsupercapacitors has been widely reported,[24−26] but the application in detection is scarce. In this work, we use this technology to prepare electrochemical sensors for the detection of lead ions.

In the electrochemical detection process, lead ions were first deposited on the electrode surface and then dissolved by DPV.[27−29] The critical step to detect heavy metal ions is the ion deposition process. High deposition efficiency will improve the sensitivity of detection. The traditional method to improve the ion deposition efficiency is usually by stirring the solution. However, it has some drawbacks, such as the generation of a non-uniform and time-dependent advection, which influences the detection signal, and it usually requires a large number of analytes. Compared with stirring in batch reactors, flow detection is easy to describe and control and requires fewer analytes. Thus, a 3D-printed reactor was prepared to realize the flow detection of lead ions.[30−34] When the electrochemical analysis is performed, the analyte flows over the electrode surface, and then the corresponding electrochemical signal can be quickly displayed. Therefore, lead ions can be effectively detected in real time.

2. RESULTS AND DISCUSSION

2.1. Characterization of the Laser-Induced Porous Carbon (LIPC). When the laser irradiates the polyimide (PI) film, PI begins to depolymerize and carbonize. Because laser sintering takes place in the atmosphere, O_2 in the air can quickly react with carbon at high temperatures to produce carbon monoxide and carbon dioxide gases. The thermolysis of the PI film also produces these gases to form pores. Therefore, the carbonization layer on the PI film has a porous structure.[35] The porous carbon was produced by laser irradiation at a power of 27 W. Characterization was performed by scanning electron microscopy (SEM), Raman spectrometry, X-ray diffraction (XRD), and Brunauer−Emmett−Teller (BET) test.

The SEM image clearly shows that the laser-induced structure has a porous morphology, as shown in Figure 1A. The cross-sectional SEM image (Figure 1B) compares the LIPC structure with the PI substrate. It can be clearly seen from the figure that the structure of PI changed significantly after decomposition and carbonization. The inset in Figure 1A shows the confocal Raman spectra of the porous carbon. The yellow line is the Raman spectrum of porous carbon on the laser-engraved track, and the blue line is the Raman spectrum of porous carbon between the two tracks. There are three strong peaks, namely, the D peak at 1352 cm^{-1}, the G peak at 1585 cm^{-1}, and the 2D peak at 2701 cm^{-1}. The D peak is

https://doi.org/10.1021/acsomega.0c06274
ACS Omega 2021, 6, 12470−12479

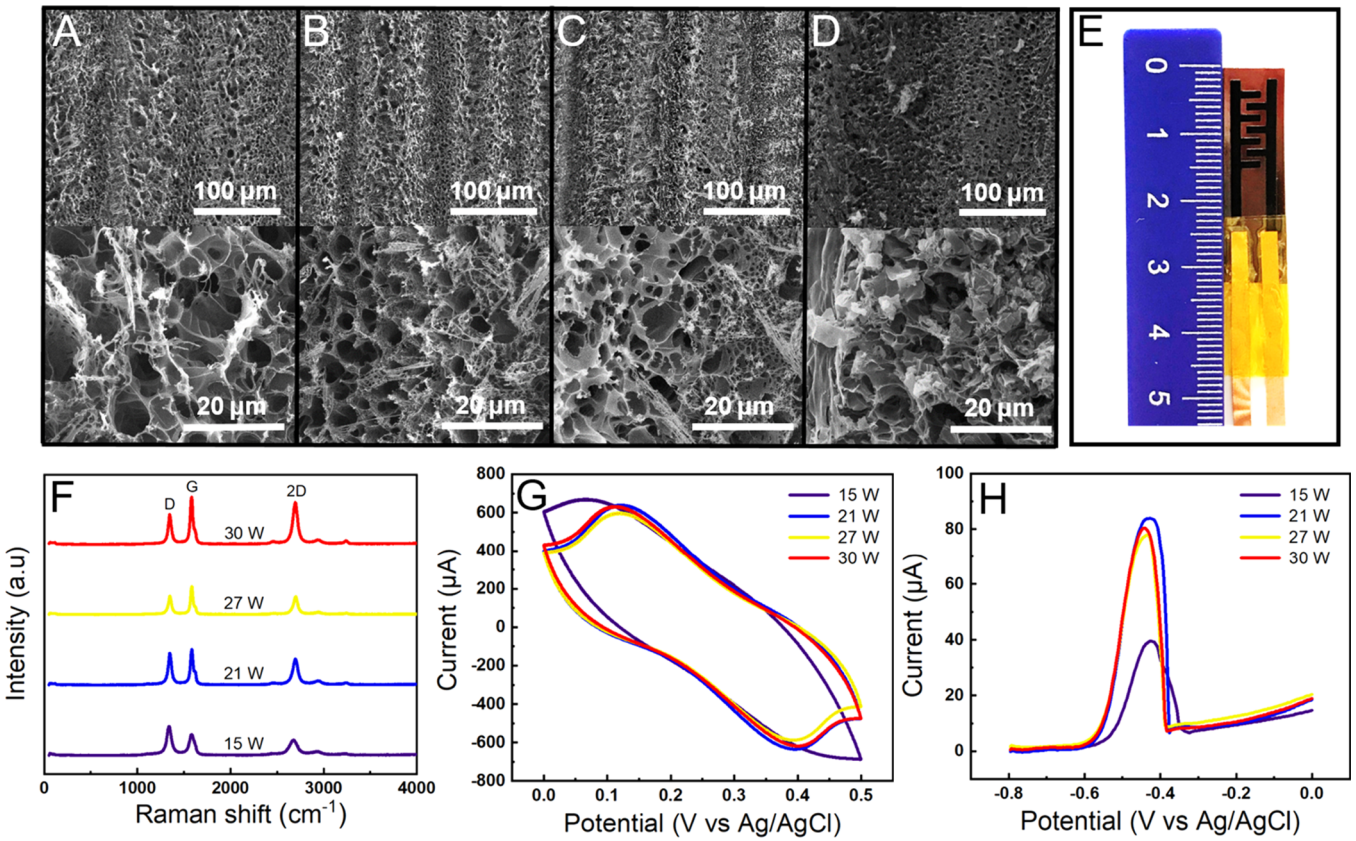

Figure 2. Optimization of the LIPCE formed at different laser powers. SEM images of LIPCs formed at different laser powers: (A) 15 W, (B) 21 W, (C) 27 W, and (D) 30 W. (E) Digital photo of the LIPCE. (F) Confocal Raman spectrometry of LIPCs with different powers. (G) CV curves of different power LIPCEs in 0.1 M KCl and 5 mM $[Fe(CN)_6]^{3-/4-}$. (H) DPV curves of different power LIPCEs in 0.4 mg/L Pb^{2+} solution (buffer: 0.1 M NaAc-HAc containing 0.1 M NaCl, pH = 4).

induced by defects or bent sp^2-carbon bonds. The G peak and 2D peak are associated with second-order zone-boundary phonons.[23] In addition, the D/G peak intensity ratio represents the graphitization degree of carbon, and the smaller the D/G peak intensity ratio is, the better the graphitization degree of carbon is. It can be seen from the figure that the graphitization degree of carbon between two laser-engraved tracks is higher than that on the laser-engraved track. This is because the sintering temperature at the laser-engraved track is very high. Excessive temperature will destroy the carbon structure, making the graphitization degree of the porous carbon in this region lower than that of the porous carbon between two laser-engraved tracks.

The XRD pattern shows two peaks at $2\theta = 25.88°$ (002) and 42.88° (100), respectively (Figure 1C). The 002 peak intensity is relatively low. It indicates that the porous substance is carbon with a low degree of graphitization. Figure 1D shows the N_2 adsorption−desorption isotherm of powdered LIPC. The inset is the pore size distribution diagram (PSD) of the sample calculated from the desorption isotherm. BET multipoint method analysis results show that the specific surface area of LIPC is 191 m^2/g, the total pore volume is 0.34 mL/g, and the average hole diameter is 7.1 nm.

2.2. Optimization of the Laser-Induced Porous Carbon Electrode (LIPCE). The power and path of laser irradiation can affect the carbonization of the PI film, which further affects the sensitivity of lead ion detection. To obtain the best electrochemical detection performance, the laser irradiating power and path were optimized.

LIPCs with powers of 15 W (LIPC15), 21 W (LIPC21), 27 W (LIPC27), and 30 W (LIPC30) were fabricated. SEM images of LIPC samples (Figure 2A−D) show the effect of laser power on the laser-induced carbon structure. The specific surface areas of LIPC15, LIPC21, LIPC27, and LIPC30 were tested by a specific surface area analyzer, and their specific surface areas are 261.476, 230.525, 215.033, and 314.867 m^2/g, respectively. The result shows that the specific surface area of LIPC30 is much larger than those of LIPC15, LIPC21, and LIPC27. It indicates that when the laser power is 30 W, more pores are formed on the surface of the PI film. LIPC15, LIPC21, LIPC27, and LIPC30 were also tested by the confocal Raman spectrometer (Figure 2F). It shows that the degree of graphitization of LIPC21, LIPC27, and LIPC30 is significantly higher than that of LIPC15.

Then, the PI films sintered with 15, 21, 27, and 30 W laser powers were made into electrodes to detect lead ions. Figure 2E shows a digital photo of the LIPCE. These electrodes were tested by CV (Figure 2G). It shows that the performance of LIPCE21, LIPCE27, and LIPCE30 is better than that of LIPCE15. Then, the electrodes were used to detect 0.4 mg/L Pb^{2+} by stripping voltammetry. Figure 2H shows the corresponding DPV curves. Compared with LIPCE15, we can see that LIPCE21, LIPCE27, and LIPCE30 are more sensitive to lead ion detection. It shows that the highly graphitized LIPC makes the concentration of lead ions deposited on the electrode surface higher and the rate of dissolution faster. The difference of their specific surface area has no effect on the electrochemical test results. There is

https://doi.org/10.1021/acsomega.0c06274
ACS Omega 2021, 6, 12470−12479

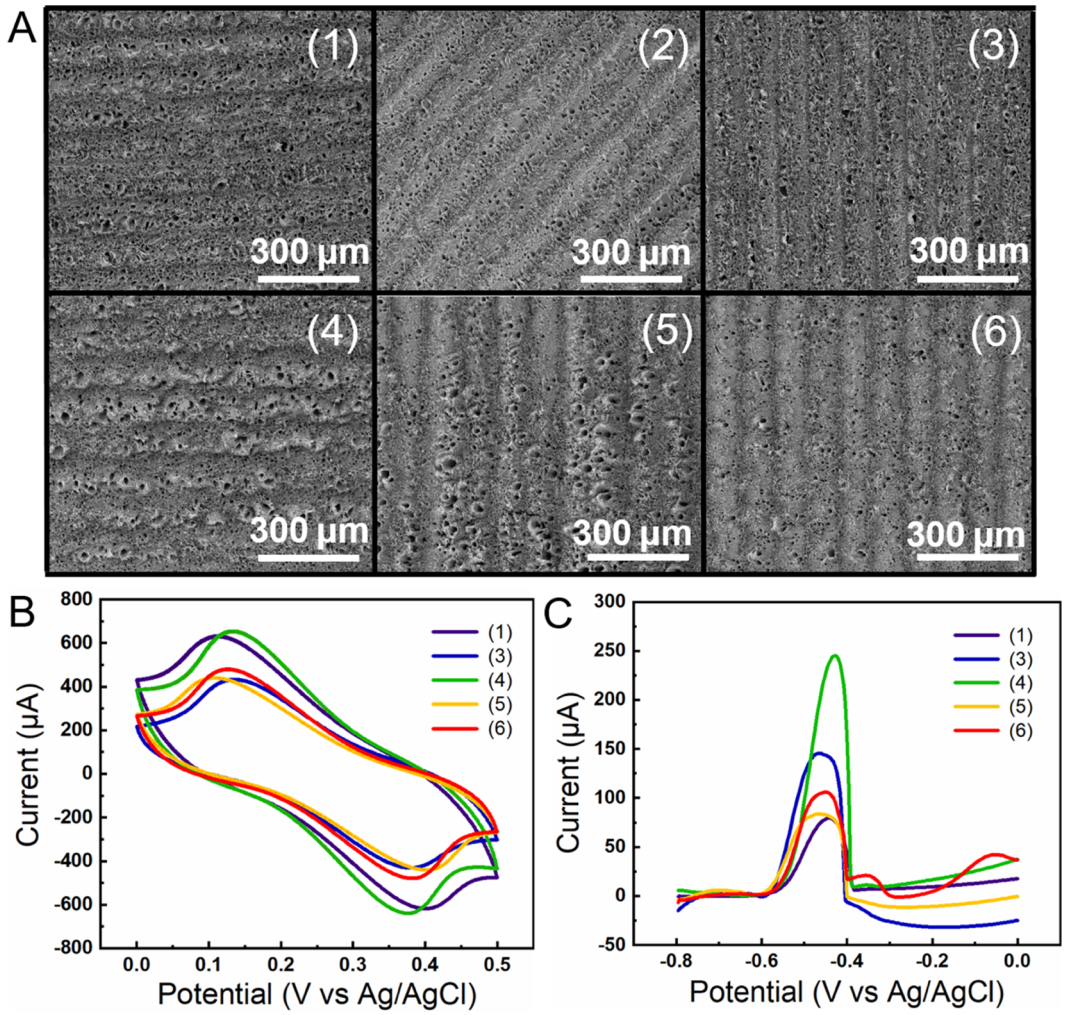

Figure 3. Optimization of LIPCE30 formed at different laser sintering paths. (A) SEM of porous carbon generated by six different laser sintering paths. (The laser sintering path of (1) was perpendicular to the long side of the electrode. The laser sintering path of (2) was at an angle of 45° to the long side of the electrode. The laser sintering path of (3) was parallel to the long side of the electrode. (4) The laser sintered the same path as (1) twice. (5) The laser sintered the same path as (3) twice. (6) The laser sintered the same path as (1) and then sintered the same path as (3).) (B) CV curves of LIPCE30 with different laser-irradiated paths in 0.1 M KCl and 5 mM $[Fe(CN)_6]^{3-/4-}$. (C) DPV curves of the LIPCE30 with different laser-irradiated paths in 0.4 mg/L Pb^{2+} solution (buffer: 0.1 M NaAc-HAc containing 0.1 M NaCl, pH = 4).

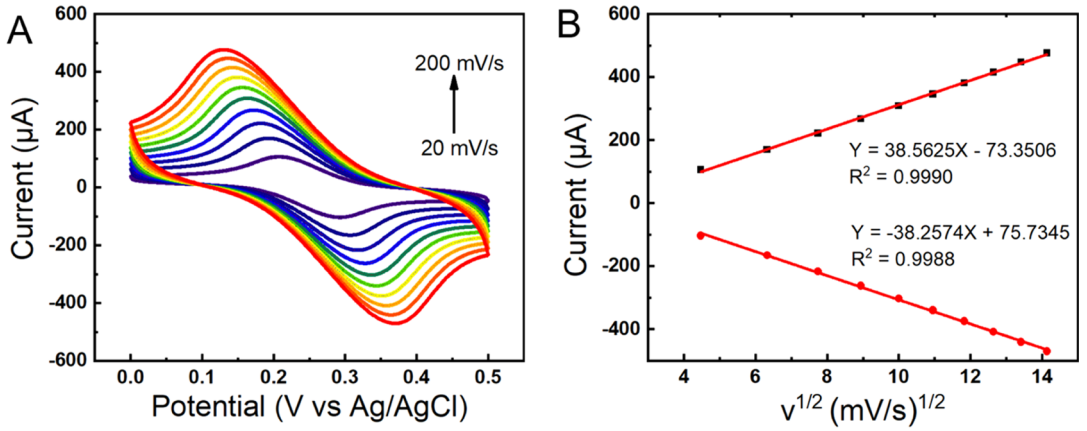

Figure 4. Electrochemical performance of LIPCE30 (4). (A) CV curves of LIPCE30 (4) in 0.1 M KCl and 5 mM $[Fe(CN)_6]^{3-/4-}$. Scan rates from 20 to 200 mV/s. (B) Plots of peak current versus the square root of the scan rate corresponding to (A).

almost no difference between LIPCE21, LIPCE27, and LIPCE30. Here, we choose LIPCE30 for the follow-up experiments.

Then, the porous carbon electrodes prepared by six different laser sintering paths were studied. The first one (1) was perpendicular to the long side of the electrode, the second one

https://doi.org/10.1021/acsomega.0c06274
ACS Omega 2021, 6, 12470−12479

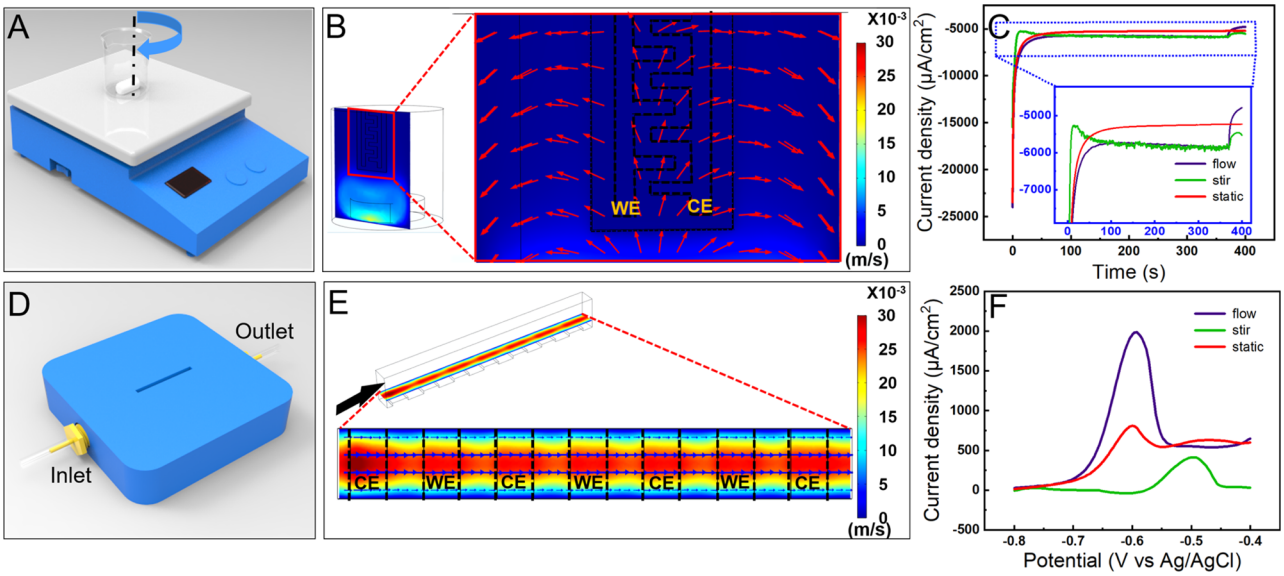

Figure 5. Numerical simulation of agitation and flow. (A) Schematic diagram of the magnetic agitator. (B, E) Velocity field distribution on the parallel surface 0.3 mm away from the electrode surface in the stirred state and flow state, respectively (unit: m/s). (C, F) i−t and DPV curves of LIPCE30 (4) in 0.4 mg/L Pb^{2+} solution, respectively (stirring rate: 300 r/min; flow rate: 2 mL/min). (D) Schematic diagram of the flow device.

(2) was at an angle of 45° to the long side of the electrode, the third one (3) was parallel to the long side of the electrode, the fourth one (4) was sintered by path (1) twice, the fifth one (5) was sintered by path (3) twice, and the sixth one (6) was sintered by path (1) and then sintered by path (3). SEM images are shown in Figure 3A. It can be seen from the figure that the porous structure of the LIPC surface sintered through paths (4) and (5) is more obvious. However, when the PI film was sintered in accordance with the designed electrode pattern, the surface of the LIPCE prepared through path (2) would be damaged. This is because the length of the sintering path is uneven and irregular, leading to uneven heating on the PI surface. This caused some porous carbon layers to warp off from the PI surface. Incomplete surfaces could negatively affect the results of electrochemical detection. Therefore, it should not be made into an electrode. The performance of other five LIPCE30 electrodes prepared by different laser irradiation paths was compared by CV (Figure 3B). It can be seen from the figure that the redox peak intensity of the fourth electrode is higher and the peak potential difference (ΔE_p) is smaller than others. It shows that the laser irradiation path (4) makes the charge transfer on the electrode surface easier and faster. Then, the sensitivity of the five electrodes to lead ion detection was compared by DPV (Figure 3C). The LIPCE30 with the laser irradiation path (4) (LIPCE30 (4)) shows the highest DPV response. It indicates that the laser irradiation path (4) makes the lead ion concentration deposited on the electrode surface higher and the dissolution rate faster. The results show that LIPCE30 (4) had excellent electrochemical performance, and we used it in the subsequent experiments.

2.3. Electrochemical Characterization of the LIPCE. The electrochemical characterization of LIPCE30 (4) was performed by CV. As shown in Figure 4A, the CVs of 5 mM $[Fe(CN)_6]^{3-/4-}$ were recorded using LIPCE30 (4) at different scan rates (20−200 mV/s). The CVs have two peaks: the oxidation peak and the reduction peak. ΔE_p is greater than 0.058 V, and i_{Pa}/i_{Pc} is greater than 1. With the increase in the scan rate, the oxidation peak position shifts to the positive direction, and the reduction peak position shifts to the negative direction. Moreover, the peak current increases with the increase in the scan rate and is proportional to the square root of the scan rate (Figure 4B). It indicates that this is a quasi-reversible electrode reaction process. In the electrode reaction, electrically active substances first reached the electrode surface through diffusion and then participated in the reaction by adsorption on the electrode surface. The relationship between the peak current and the square root of the scan rate is linear, which indicates that the electrode process was mainly controlled by diffusion. The electrochemical surface area (ECSA) of LIPCE30 (4) was estimated by the Randles−Sevčik equation:[36−41]

$$I_p = 2.69 \times 10^5 A D^{1/2} n^{3/2} v^{1/2} C$$

where I_p is the peak current, A is the effective surface area, D is the diffusion coefficient of $K_3Fe(CN)_6$ (7.6×10^{-6} cm^2/s), n is the number of electrons transferred ($n = 1$), v is the scan rate, and C is the concentration of $K_3Fe(CN)_6$. For LIPCE30 (4), the ECSA is about 0.3275 cm^2.

2.4. Optimization of Analytical Conditions. Determining the best experimental conditions was the key to obtain the highest detection sensitivity.[21] The analytical conditions were optimized before evaluating the electrochemical detection performance of LIPCE30 (4).

The enrichment process has a great influence on the detection sensitivity of lead ions, and usually, the solution must be stirred to reduce the thickness of the diffusion layer. The flow of the solution allows the lead ions to effectively approach the electrode surface and more easily adsorb on the porous carbon electrode. Here, we used a flow reactor to make the liquid flow. The velocity distribution near the electrode surface was simulated numerically when the electrode was in batch and flow reactors (Figure 5). It can be seen that agitation leads to uneven dynamics, and mass transfer is mainly limited to the liquid phase far away from the solid phase (Figure 5B), which is not beneficial for the adsorption of the ions. However, in the flow reactor, the flow of solution can not only produce more stable advection in a controlled and predictable manner, but

https://doi.org/10.1021/acsomega.0c06274
ACS Omega 2021, 6, 12470−12479

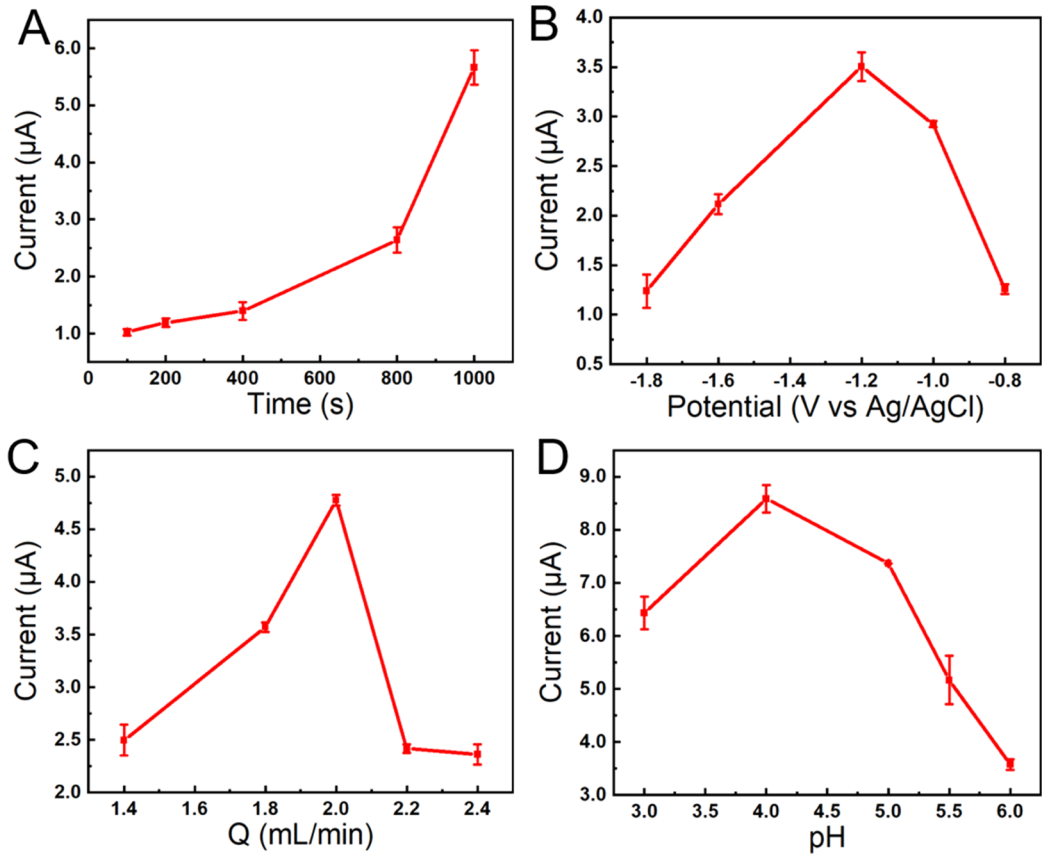

Figure 6. Optimization of electrochemical analytical conditions. Plot of the DPV peak current curve versus (A) deposition time, (B) deposition potential, (C) analyte flow rate, and (D) buffer pH.

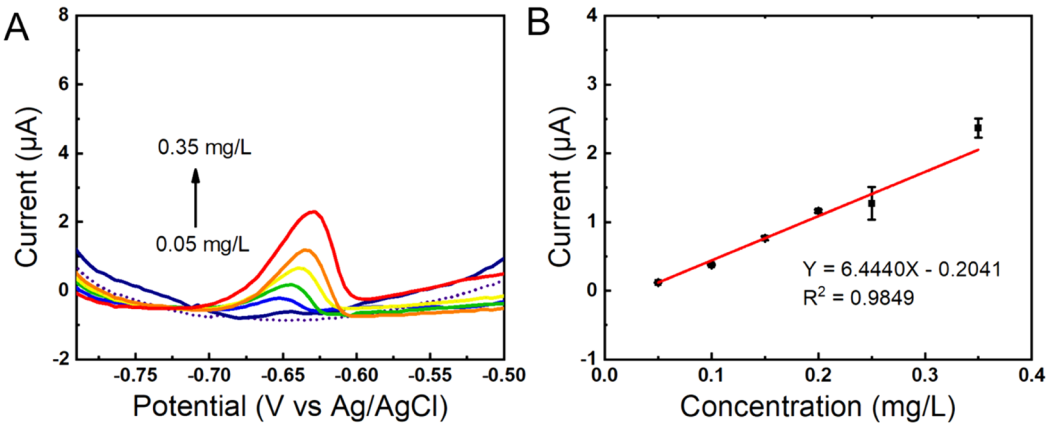

Figure 7. Analytical performance of the sensor toward Pb^{2+} detection. (A) DPV recordings obtained for increasing concentrations of Pb^{2+} (0.05−0.35 mg/L) at LIPCE30 (4) in 0.1 M NaAc-HAc containing 0.1 M NaCl (pH = 4). Deposition potential: −1.2 V; deposition time: 200 s; flow rate of the analyte: 2 mL/min. (B) The calibration curve corresponded to (A).

more importantly, it can also effectively improve surface dynamics (Figure 5E).

It can be seen from Figure 5C that the *i*−*t* curve in the flowing state is much smoother than that in the stirring state, which indicates that the stirring of the solution will cause current fluctuations and unstable deposition of lead ions. However, the solution's flow keeps the analyte on the electrode surface always in a new state, and lead ions can be stably deposited on the electrode surface and generate a stable current. It can be seen from Figure 5F that the detection sensitivity of the electrode to lead ions in the flow state is higher than that in the stirred and static states. Therefore, flow detection was adopted in the following experiments.

The deposition time from 100 to 1000 s was studied (Figure 6A). The peak current increases with the increase in electrodeposition time, which indicates that extending the electrodeposition time can improve the sensitivity of lead ion detection. But with the increase in electrodeposition time, the linear relationship will become worse. Therefore, we choose 200 s as the best electrodeposition time. The deposition potential from −1.8 to −0.8 V was studied (Figure 6B). The peak current increases significantly from −1.8 to −1.2 V and

https://doi.org/10.1021/acsomega.0c06274
ACS Omega 2021, 6, 12470−12479

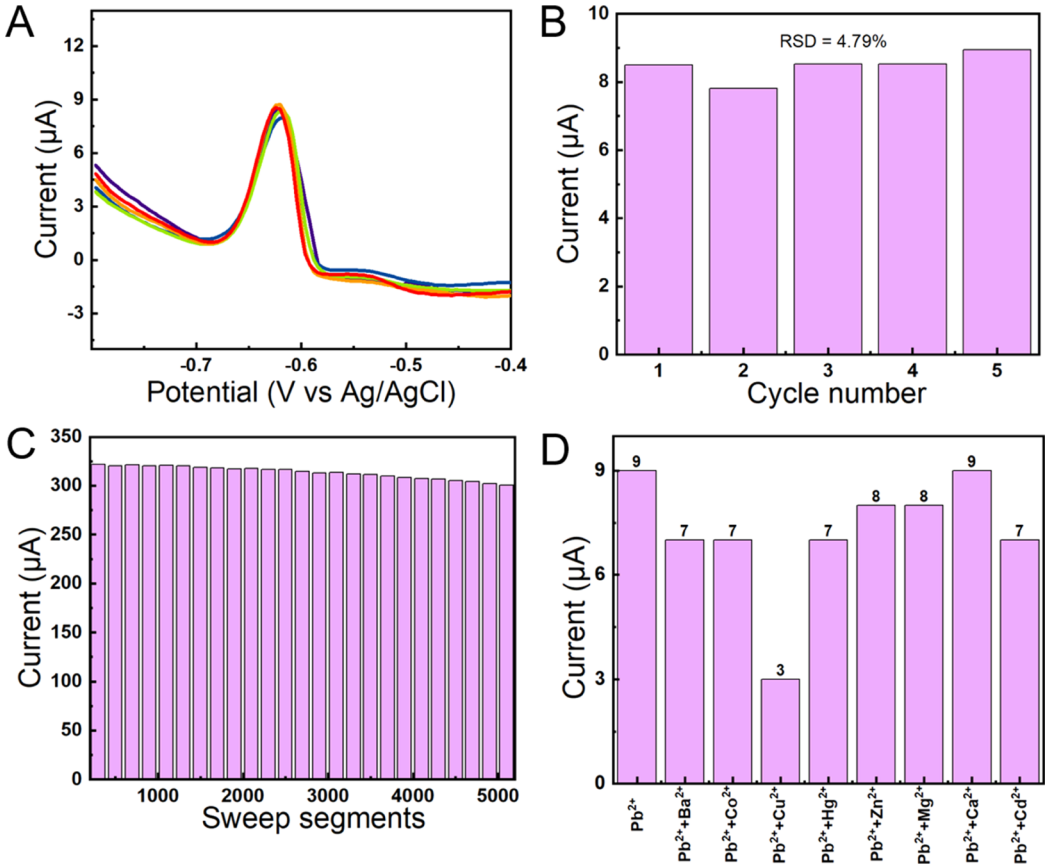

Figure 8. Reproducibility, stability, and anti-interference studies. (A) Five DPV recordings of Pb^{2+} (0.4 mg/L) at the same LIPCE30 (4) in 0.1 M NaAc-HAc containing 0.1 M NaCl (pH = 4). (B) Plot of peak current versus the cycle number corresponding to (A). (C) Plot of CV oxidation peak current versus sweep segments in 0.1 M KCl containing 5 mM $[Fe(CN)_6]^{3-/4-}$. (D) Anti-interference study of LIPCE30 (4) to 0.4 mg/L Pb^{2+} in the presence of 4 mg/L Ba^{2+}, Co^{2+}, Cu^{2+}, Hg^{2+}, Zn^{2+}, Mg^{2+}, Ca^{2+}, and Cd^{2+}.

reaches a maximum at −1.2 V, and then, the current decreases. So, −1.2 V was selected as the optimal deposition potential. Similarly, the flow rate of the analyte from 1.4 to 2.4 mL/min was studied (Figure 6C). The DPV response peak current increases with increasing flow rate and reaches a maximum at 2 mL/min. Then, the current drops significantly. When the flow rate is less than 2 mL/min, the deposition amount of lead ions increases with the increase in the flow rate. When the flow rate is more than 2 mL/min, the lead ion cannot be deposited effectively due to the high flow rate. So, the flow rate of 2 mL/min was selected for this work. Then, the pH of the buffer was optimized. Figure 6D shows the effect of NaAc-HAc buffer pH on electrochemical behavior. The response peak current of the DPV curve increases with the increase in the pH value and reaches the maximum at pH = 4. Then, the current gradually decreases. When the pH of the buffer increases, the concentration of OH^- in the solution also increases. OH^- will react with Pb^{2+}, leading to a decrease in the concentration of lead ions in the solution. So, the DPV response peak current goes down. Therefore, the buffer solution with pH = 4 was selected for the experiment.

2.5. Analytical Performance of the Sensor toward Pb^{2+} Detection. To realize the quantitative detection of Pb^{2+}, the sensor detected different concentrations of Pb^{2+} through DPV measurement. LIPCE30 (4) was used as the electrode, and the experiment was performed under the optimized conditions. Figure 7A shows the DPV curves for the concentrations from 0.05 to 0.35 mg/L. Figure 7B shows that peak currents are linearly related to the concentrations of Pb^{2+}, and the corresponding calibration curve is $y = 6.4440x - 0.2041$ ($R^2 = 0.9849$). The limit of detection (LOD) is estimated to be 0.0330 mg/L for Pb^{2+}.

2.6. Reproducibility, Stability, and Anti-interference Studies. The reproducibility of LIPCE30 (4) was evaluated by 5 times DPV measurements of 0.4 mg/L Pb^{2+} (Figure 8A). The relative standard deviation (RSD) is 4.79% (Figure 8B). It indicates that the reproducibility of LIPCE30 (4) is good. The stability of LIPCE30 (4) was evaluated by CV measurement in a 5 mM $[Fe(CN)_6]^{3-/4-}$ solution containing 0.1 M KCl. Figure 8C shows that the CV oxidation peak current changes little within 5000 sweep segments, indicating that LIPCE30 (4) has high stability. To study the anti-interference of LIPCE30 (4), some possible interfering metal ions were added into 0.4 mg/L Pb^{2+}. These ions were 10 times more concentrated than lead ions. It can be seen from Figure 8D that these metal ions have little interference with Pb^{2+} except for Cu^{2+}. When the interference of Cu^{2+} to lead ion detection was studied, the oxidation peak of Cu^{2+} would also appear. It indicated that Cu^{2+} and Pb^{2+} were deposited together on the electrode surface when the deposition potential was −1.2 V. Then, Cu^{2+} would be dissolved together with Pb^{2+}. So, the lead ion has a lower response peak current. However, lead ions still can be detected in the presence of Cu^{2+}. These characteristics make LIPCE30 (4) have a broad application prospect in electrochemical detection.

https://doi.org/10.1021/acsomega.0c06274
ACS Omega 2021, 6, 12470−12479

Scheme 1. Procedure of Electrochemical Analysis[a]

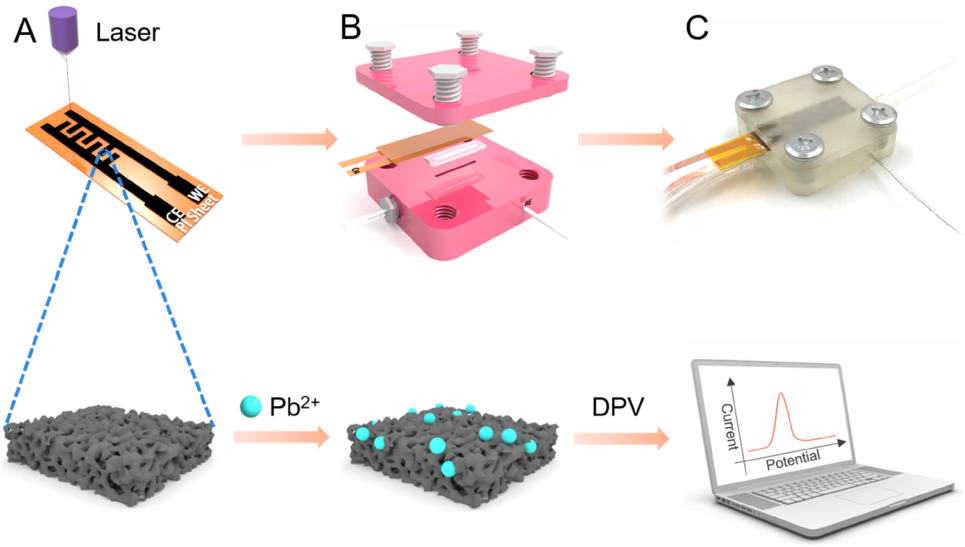

[a](A) Laser sintering process; (B, C) schematic and digital photographs of the electrochemical sensor, respectively.

3. CONCLUSIONS

In conclusion, we reported a low-cost, direct laser sintering method for electrode preparation. The electrode can detect lead ions quickly and efficiently. The laser irradiation power and path significantly affect the electrochemical performance of LIPCE. The best laser irradiation power and path were obtained through optimization. According to the electrochemical characterization, the electrode process was controlled by diffusion. The electrochemical deposition was usually carried out in the state of agitation. To compare the effects of agitation and flow on electrochemical detection, the velocity distribution near the electrode surface under stirring and flowing conditions was simulated numerically. Simulation results showed that the laminar flow in a continuous flow reactor was more beneficial to the improvement of electrode surface dynamics than stirring in a batch reactor, and electrochemical experiments also showed that flow detection had higher sensitivity. Under the optimal experimental conditions, the sensor was used for the quantitative analysis of Pb^{2+}. The estimated LOD was 0.0330 mg/L. The study also proved that LIPCE30 (4) had good stability and repeatability. Therefore, the sensor was expected to be widely used for more electrochemical detections.

4. EXPERIMENTAL SECTION

4.1. Materials and Reagents. PI was obtained from Changchun Gao Qi Polyimide Material Co., Ltd. $Co(NO_3)_2 \cdot 6H_2O$, $K_3[Fe(CN)_6]$, $K_4Fe(CN)_6 \cdot 3H_2O$, CH_3COONa, CH_3COOH, HCl, and KCl were bought from Tianjin Kemiou Chemical Reagent Corp. $Mg(NO_3)_2 \cdot 6H_2O$, $Ba(NO_3)_2$, and $Pb(NO_3)_2$ were received from the Shanghai Aladdin Biochem Technology Corp. $Zn(NO_3)_2 \cdot 6H_2O$ and $Ca(NO_3)_2 \cdot 4H_2O$ were purchased from Damao Chemical Reagent Factory (Tianjin, China). NaCl and $Cd(NO_3)_2 \cdot 4H_2O$ were obtained from Shanghai Macleans Biochemical Technology Co., Ltd. $(CH_3COO)_2Cu \cdot H_2O$ was bought from Sinopharm Chemical Reagent Co., Ltd. $Hg(NO_3)_2 \cdot H_2O$ was received from West Asia Chemical Technology (Shandong) Co., Ltd. The copper sheet was bought from Shanghai Lujiang Hardware. Silver wire (1.0 mm in diameter, annealed, 99.9%, metal basis) was obtained from Alfa Aesar Chemical Co., Ltd. Epoxy adhesive (Devcon 14250) was obtained from Shenzhen Darbond Technology Co., Ltd. Deionized water was used for all of the experiments.

4.2. Preparation of the Working Electrode (WE), Conference Electrode (CE), and Ag/AgCl Reference Electrode (RE). Both WE and CE were manufactured by laser sintering on PI films (Scheme 1A). Using a CO_2 laser (marking speed: 400 mm/s; frequency: 15 kHz; resolution: 0.001 mm; repeated positioning accuracy: 0.003 mm), the PI film was converted into a porous carbon electrode with a design pattern (7.48 × 28.05 mm). The RE was prepared by an electroplating method. First, the silver wire was ultrasonically cleaned in alcohol for 30 min and rinsed with deionized water. It was then electroplated for 30 min in a 0.1 M HCl solution by chronopotentiometry, with commercial Ag/AgCl as the RE and Pt as the CE. The silver wire was coated with AgCl at last, and we obtained the Ag/AgCl RE.

4.3. Assembly of the 3D-Printed Flow Reactor and Electrodes. We used Solidworks to design the reactor structure and imported the STL files into a 3D printer. The reactor can be accurately manufactured with the 3D printer at a high resolution of 50 μm. The flow reactor structure with the reaction channel is schematically illustrated in Scheme 1B. The reaction channel is 14 mm in length, 1 mm in depth, and 1 mm in width. A hole (r = 0.65 mm) for the RE was made on the longer side of the channel.

The Ag/AgCl RE was fixed in the reactor with epoxy adhesive. The PI film with the WE and CE was fixed between the silicon gasket and the higher flange. The whole device was then fixed with screws. The copper sheets, which were fixed on the edge of both WE and CE with conductive silver glue, were used to ensure good contact between the sensor and the electrochemical workstation. Scheme 1B,C shows schematic and digital photographs of the electrochemical sensor, respectively. The inlet and outlet of the channel were connected by hoses. The inlet hose was then connected to a syringe pump.

4.4. Electrochemical Measurements. A three-electrode system was used in all experiments. The electrodes were

https://doi.org/10.1021/acsomega.0c06274
ACS Omega 2021, 6, 12470−12479

characterized by CV in 0.1 M KCl containing 5 mM $[Fe(CN)_6]^{3-/4-}$. Except for special declarations, the scanning rate of the CV test was 0.1 V/s. The lead ions were determined by DPV. The pulse width was 0.05 s, the pulse period was 0.5 s, and the pulse amplitude was 0.05 V.

4.5. Calibration Experiments. The RSD between the electrodes can be solved by calibration experiments. First, we use electrode A to obtain the standard curve and its peak current (I_{PA}) in 0.4 mg/L Pb^{2+} solution. For the other electrode B, we can also obtain its peak current (I_{PB}) in 0.4 mg/L Pb^{2+} solution. I_{PA}/I_{PB} is the correction factor (σ). When using the B electrode to detect the sample, the corresponding peak current (I_{PI}) is obtained. $I_{PI} \times \sigma$ is the peak current of the A electrode for the sample, and then the concentration of the sample is obtained from the standard curve.

4.6. Characterization. SEM images were obtained by a QUANTA 450 scanning electron microscope at 20 kV. The pore properties were surveyed by an ASAP 2010 analysis instrument at 77 K. The specific surface areas were calculated by the BET method, and the pore size was calculated using the Barrett−Joyner−Halenda (BJH) model. XRD patterns were measured on a Rigaku D/MAX-2400 X-ray powder diffractometer (Japan) operating at 40 kV and 100 mA using Cu Kα radiation. The Raman spectra were recorded with a Nicolet Almega XR Raman system with a 532 nm laser. LIPC was obtained by a CO_2 laser (Coherent C series 30 W, 10.6 μm wavelength). The injector containing the analyte was controlled by a syringe pump (Leifu, TYD03-01). The electrochemical performance of the LIPCE was studied using CV and DPV on a CHI model 660D electrochemical workstation (CH Instrument, Inc.). The flow reactor was produced by 3D printing from stereolithography resin (methacrylate photopolymer resin, Formlabs Form 2, 0.05 mm layer resolution).

AUTHOR INFORMATION

Corresponding Author

Shengyang Tao − *Department of Chemistry, School of Chemical Engineering, Dalian University of Technology, Dalian 116024, Liaoning, P.R. China;* orcid.org/0000-0002-0567-8860; Email: taosy@dlut.edu.cn

Authors

Baojun Ding − *Department of Chemistry, School of Chemical Engineering, Dalian University of Technology, Dalian 116024, Liaoning, P.R. China*

Qiunan Zhang − *Department of Chemistry, School of Chemical Engineering, Dalian University of Technology, Dalian 116024, Liaoning, P.R. China*

Cheng Yang − *Department of Chemistry, School of Chemical Engineering, Dalian University of Technology, Dalian 116024, Liaoning, P.R. China*

Wenbo Yang − *Department of Chemistry, School of Chemical Engineering, Dalian University of Technology, Dalian 116024, Liaoning, P.R. China;* orcid.org/0000-0003-2156-0560

Junbo Liu − *Department of Chemistry, School of Chemical Engineering, Dalian University of Technology, Dalian 116024, Liaoning, P.R. China*

Chong Li − *Department of Chemistry, School of Chemical Engineering, Dalian University of Technology, Dalian 116024, Liaoning, P.R. China*

Complete contact information is available at: https://pubs.acs.org/10.1021/acsomega.0c06274

Author Contributions

‡B.D., Q.Z., and C.Y. contributed equally to this work.

Notes

The authors declare no competing financial interest.

ACKNOWLEDGMENTS

The authors acknowledge the financial support from the National Natural Science Foundation of China (21872018 and 21107008) and the Fundamental Research Funds for the Central Universities (no. DUT20GJ208).

REFERENCES

(1) Cheng, S. Heavy metal pollution in China: origin, pattern and control. *Environ. Sci. Pollut. Res.* **2003**, *10*, 192−198.

(2) Yang, D.; Liu, X.; Zhou, Y.; Luo, L.; Zhang, J.; Huang, A.; Mao, Q.; Chen, X.; Tang, L. Aptamer-based biosensors for detection of lead(II) ion: a review. *Anal. Methods* **2017**, *9*, 1976−1990.

(3) Godwin, H. A. The biological chemistry of lead. *Curr. Opin. Chem. Biol.* **2001**, *5*, 223−227.

(4) Townsend, A. T.; Miller, K. A.; McLean, S.; Aldous, S. The determination of copper, zinc, cadmium and lead in urine by high resolution ICP-MS. *J. Anal. At. Spectrom.* **1998**, *13*, 1213−1219.

(5) Kumar, B. N.; Ramana, D. K.; Harinath, Y.; Seshaiah, K.; Wang, M. C. Separation and preconcentration of Cd(II), Cu(II), Ni(II), and Pb(II) in water and food samples using Amberlite XAD-2 functionalized with 3-(2-nitrophenyl)-1H-1,2,4-triazole-5(4H)-thione and determination by inductively coupled plasma-atomic emission spectrometry. *J. Agric. Food Chem.* **2011**, *59*, 11352−11358.

(6) Han, Y.; Li, Y.; Si, W.; Wei, D.; Yao, Z.; Zheng, X.; Du, B.; Wei, Q. Simultaneous determination of Cu^{2+}, Zn^{2+}, Cd^{2+}, Hg^{2+} and Pb^{2+} by using second-derivative spectrophotometry method. *Spectrochim. Acta, Part A* **2011**, *79*, 1546−1551.

(7) Liu, J.; Chen, H.; Mao, X.; Jin, X. Determination of trace copper, lead, cadmium, and iron in environmental and biological samples by flame atomic absorption spectrometry coupled to flow injection on-line coprecipitation preconcentration using DDTC-nickel as coprecipitate carrier. *Int. J. Environ. Anal. Chem.* **2000**, *76*, 267−282.

(8) Zhang, H.; Jiang, B.; Xiang, Y.; Su, J.; Chai, Y.; Yuan, R. DNAzyme-based highly sensitive electronic detection of lead via quantum dot-assembled amplification labels. *Biosens. Bioelectron.* **2011**, *28*, 135−138.

(9) Chen, L.; Su, Z.; He, X.; Liu, Y.; Qin, C.; Zhou, Y.; Li, Z.; Wang, L.; Xie, Q.; Yao, S. Square wave anodic stripping voltammetric determination of Cd and Pb ions at a Bi/Nafion/thiolated polyaniline/glassy carbon electrode. *Electrochem. Commun.* **2012**, *15*, 34−37.

(10) Cui, L.; Wu, J.; Ju, H. Electrochemical sensing of heavy metal ions with inorganic, organic and bio-materials. *Biosens. Bioelectron.* **2015**, *63*, 276−286.

(11) Saidur, M. R.; Aziz, A. A.; Basirun, W. J. Recent advances in DNA-based electrochemical biosensors for heavy metal ion detection: A review. *Biosens. Bioelectron.* **2017**, *90*, 125−139.

(12) Hu, C.; Zhang, Y.; Bao, G.; Zhang, Y.; Liu, M.; Wang, Z. L. DNA functionalized single-walled carbon nanotubes for electrochemical detection. *J. Phys. Chem. B.* **2005**, *109*, 20072−20076.

(13) Pollok, N. E.; Rabin, C.; Walgama, C. T.; Smith, L.; Richards, I.; Crooks, R. M. Electrochemical detection of NT-proBNP using a metalloimmunoassay on a paper electrode platform. *ACS Sens.* **2020**, *5*, 853−860.

(14) Rajendran, S. T.; Scarano, E.; Bergkamp, M. H.; Capria, A. M.; Cheng, C.-H.; Sanger, K.; Ferrari, G.; Nielsen, L. H.; Hwu, E.-T.; Zór, K.; Boisen, A. Modular, lightweight, wireless potentiostat-on-a-Disc for electrochemical detection in centrifugal microfluidics. *Anal. Chem.* **2019**, *91*, 11620−11628.

(15) Madigan, N. A.; Murphy, T. J.; Fortune, J. M.; Hagan, C. R. S.; Coury, L. A. Sonochemical stripping voltammetry. *Anal. Chem.* **1995**, *67*, 2781−2786.
(16) Simoska, O.; Sans, M.; Fitzpatrick, M. D.; Crittenden, C. M.; Eberlin, L. S.; Shear, J. B.; Stevenson, K. J. Real-time electrochemical detection of pseudomonas aeruginosa phenazine metabolites using transparent carbon ultramicroelectrode arrays. *ACS Sens.* **2019**, *4*, 170−179.
(17) Zhou, W. Y.; Li, S. S.; Song, J. Y.; Jiang, M.; Jiang, T. J.; Liu, J. Y.; Liu, J. H.; Huang, X. J. High electrochemical sensitivity of TiO_{2-x} nanosheets and an electron-induced mutual interference effect toward heavy metal ions demonstrated using X-ray absorption fine structure spectra. *Anal. Chem.* **2018**, *90*, 4328−4337.
(18) Lu, M.; Deng, Y.; Luo, Y.; Lv, J.; Li, T.; Xu, J.; Chen, S. W.; Wang, J. Graphene aerogel-metal-organic framework-based electrochemical method for simultaneous detection of multiple heavy-metal ions. *Anal. Chem.* **2019**, *91*, 888−895.
(19) Dong, S.; Wang, Z.; Asif, M.; Wang, H.; Yu, Y.; Hu, Y.; Liu, H.; Xiao, F. Inkjet printing synthesis of sandwiched structured ionic liquid-carbon nanotube-graphene film: toward disposable electrode for sensitive heavy metal detection in environmental water samples. *Ind. Eng. Chem. Res.* **2017**, *56*, 1696−1703.
(20) Ottakam Thotiyl, M. M.; Freunberger, S. A.; Peng, Z.; Bruce, P. G. The carbon electrode in nonaqueous Li-O_2 cells. *J. Am. Chem. Soc.* **2013**, *135*, 494−500.
(21) Alam, A. U.; Deen, M. J. Bisphenol A electrochemical sensor using graphene oxide and beta-cyclodextrin-functionalized multiwalled carbon nanotubes. *Anal. Chem.* **2020**, *92*, 5532−5539.
(22) Lee, G. J.; Pyun, S. I. Theoretical approach to ion penetration into pores with pore fractal characteristics during double-layer charging/discharging on a porous carbon electrode. *Langmuir* **2006**, *22*, 10659−10665.
(23) Lin, J.; Peng, Z.; Liu, Y.; Ruiz-Zepeda, F.; Ye, R.; Samuel, E. L. G.; Yacaman, M. J.; Yakobson, B. I.; Tour, J. M. Laser-induced porous graphene films from commercial polymers. *Nat. Commun.* **2014**, *5*, 5714.
(24) El-Kady, M. F.; Kaner, R. B. Scalable fabrication of high-power graphene micro-supercapacitors for flexible and on-chip energy storage. *Nat. Commun.* **2013**, *4*, 1475.
(25) Song, W.; Zhu, J.; Gan, B.; Zhao, S.; Wang, H.; Li, C.; Wang, J. Flexible, stretchable, and transparent planar microsupercapacitors based on 3D porous laser-induced graphene. *Small* **2018**, *14*, 1702249.
(26) Liu, J.; Zhang, L.; Yang, C.; Tao, S. Preparation of multifunctional porous carbon electrodes through direct laser writing on a phenolic resin film. *J. Mater. Chem. A* **2019**, *7*, 21168−21175.
(27) Bui, M.-P. N.; Brockgreitens, J.; Ahmed, S.; Abbas, A. Dual detection of nitrate and mercury in water using disposable electrochemical sensors. *Biosens. Bioelectron.* **2016**, *85*, 280−286.
(28) Prashanth, S. A.; Pandurangappa, M. Amino-calix[4]arene modified graphite as an electrochemical interface for mercury(II) quantification. *Mater. Lett.* **2016**, *185*, 476−479.
(29) Han, J.; Fu, R.; Jin, C.; Li, Z.; Wang, M.; Yu, P.; Xie, Y. Highly sensitive detection of trace Hg^{2+} via PdNPs/g-C_3N_4 nanosheet-modified electrodes using DPV. *Microchem. J.* **2020**, *152*, 104356.
(30) Bagheri, A.; Jin, J. Photopolymerization in 3D printing. *ACS Appl. Polym. Mater.* **2019**, *1*, 593−611.
(31) Au, A. K.; Huynh, W.; Horowitz, L. F.; Folch, A. 3D-printed microfluidics. *Angew. Chem., Int. Ed. Engl.* **2016**, *55*, 3862−3881.
(32) Ambrosi, A.; Moo, J. G. S.; Pumera, M. Helical 3D-printed metal electrodes as custom-shaped 3D platform for electrochemical devices. *Adv. Funct. Mater.* **2016**, *26*, 698−703.
(33) Bettermann, S.; Schroeter, B.; Moritz, H.-U.; Pauer, W.; Fassbender, M.; Luinstra, G. A. Continuous emulsion copolymerization processes at mild conditions in a 3D-printed tubular bended reactor. *Chem. Eng. J.* **2018**, *338*, 311−322.
(34) Peris, E.; Okafor, O.; Kulcinskaja, E.; Goodridge, R.; Luis, S. V.; Garcia-Verdugo, E.; O'Reilly, E.; Sans, V. Tuneable 3D printed bioreactors for transaminations under continuous-flow. *Green Chem.* **2017**, *19*, 5345−5349.
(35) Zhang, Y.; Li, N.; Xiang, Y.; Wang, D.; Zhang, P.; Wang, Y.; Lu, S.; Xu, R.; Zhao, J. A flexible non-enzymatic glucose sensor based on copper nanoparticles anchored on laser-induced graphene. *Carbon* **2020**, *156*, 506−513.
(36) Abdel-Aziz, A. M.; Hassan, H. H.; Badr, I. H. A. Glassy carbon electrode electromodification in the presence of organic monomers: electropolymerization versus activation. *Anal. Chem.* **2020**, *92*, 7947−7954.
(37) Kim, K. J.; Lee, H. S.; Kim, J.; Park, M. S.; Kim, J. H.; Kim, Y. J.; Skyllas-Kazacos, M. Superior electrocatalytic activity of a robust carbon-felt electrode with oxygen-rich phosphate groups for all-vanadium redox flow batteries. *ChemSusChem* **2016**, *9*, 1329−1338.
(38) Lee, J.; Park, M. S.; Kim, K. J. Highly enhanced electrochemical activity of Ni foam electrodes decorated with nitrogen-doped carbon nanotubes for non-aqueous redox flow batteries. *J. Power Sources* **2017**, *341*, 212−218.
(39) Flox, C.; Rubio-Garcia, J.; Nafria, R.; Zamani, R.; Skoumal, M.; Andreu, T.; Arbiol, J.; Cabot, A.; Morante, J. R. Active nano-$CuPt_3$ electrocatalyst supported on graphene for enhancing reactions at the cathode in all-vanadium redox flow batteries. *Carbon* **2012**, *50*, 2372−2374.
(40) Park, M.; Jung, Y. J.; Kim, J.; Lee, H. I.; Cho, J. Synergistic effect of carbon nanofiber/nanotube composite catalyst on carbon felt electrode for high-performance all-vanadium redox flow battery. *Nano Lett.* **2013**, *13*, 4833−4839.
(41) Lee, K.; Lee, J.; Kwon, K. W.; Park, M. S.; Hwang, J. H.; Kim, K. J. 3D graphene−Ni foam as an advanced electrode for high-performance nonaqueous redox flow batteries. *ACS Appl. Mater. Interfaces* **2017**, *9*, 22502−22508.

https://doi.org/10.1021/acsomega.0c06274
ACS Omega 2021, 6, 12470−12479